


The role of binarity and stellar rotation in the split main sequence of NGC 2422

CHENYU HE (贺辰昱) ^{1,2} WEIJIA SUN (孙唯佳) ^{3,4} CHENGYUAN LI (李程远) ^{1,2} LU LI (李璐) ^{5,6,7}
ZHENGYI SHAO (邵正义) ^{5,8} JING ZHONG (钟靖) ⁵ LI CHEN (陈力) ^{5,6} RICHARD DE GRUJS ^{9,10}
BAITIAN TANG (汤柏添) ^{1,2} SONGMEI QIN (秦松梅) ^{5,6} AND ZARA RANDRIAMANAKOTO ^{11,12}

¹*School of Physics and Astronomy, Sun Yat-sen University, Zhuhai, 519082, China*

²*CSST Science Center for the Guangdong–Hong Kong–Macau Greater Bay Area, Zhuhai, 519082, China*

³*Department of Astronomy, Peking University, Yi He Yuan Lu 5, Hai Dian District, Beijing, 100871, China*

⁴*CAS Key Laboratory of Optical Astronomy, National Astronomical Observatories, Chinese Academy of Sciences, Beijing 100101, China*

⁵*Key Laboratory for Research in Galaxies and Cosmology, Shanghai Astronomical Observatory, Chinese Academy of Sciences, 80 Nandan Road, Shanghai, 200030, China*

⁶*School of Astronomy and Space Science, University of Chinese Academy of Sciences, 19A Yuquan Road, Beijing, 100049, China*

⁷*Centre for Astrophysics and Planetary Science, Racah Institute of Physics, The Hebrew University, Jerusalem, 91904, Israel*

⁸*Key Laboratory for Astrophysics, Chinese Academy of Sciences, Shanghai 200234, China*

⁹*School of Mathematical and Physical Sciences, Macquarie University, Balaclava Road, Sydney, NSW 2109, Australia*

¹⁰*Research Centre for Astronomy, Astrophysics and Astrophotonics, Macquarie University, Balaclava Road, Sydney, NSW 2109, Australia*

¹¹*South African Astronomical Observatory, P.O. Box 9, Observatory, Cape Town 7935, South Africa*

¹²*Department of Physics, University of Antananarivo, P.O. Box 906, Antananarivo, Madagascar*

(Dated: August 2022)

ABSTRACT

In addition to the extended main-sequence turnoffs widely found in young and intermediate-age (~ 600 Myr–2 Gyr-old) star clusters, some younger clusters even exhibit split main sequences (MSs). Different stellar rotation rates are proposed to account for the bifurcated MS pattern, with red and blue MSs (rMS and bMS) populated by fast and slowly rotating stars, respectively. Using photometry from *Gaia* Early Data Release 3, we report a Galactic open cluster with a bifurcated MS, NGC 2422 (~ 90 Myr). We exclude the possibilities that the bifurcated MS pattern is caused by photometric noise or differential reddening. We aim to examine if stellar rotation can account for the split MS. We use spectra observed with the Canada–France–Hawaii Telescope and the Southern African Large Telescope, and directly measured $v \sin i$, the projected rotational velocities, for stars populating the bMS and rMS. We find that their $v \sin i$ values are weakly correlated with their loci in the color–magnitude diagram because of contamination caused by a large fraction of rMS stars with low projected rotational velocities. Based on the spectral energy distribution fitting method, we suggest that these slowly rotating stars at the rMS may hide a binary companion, which breaks the expected $v \sin i$ –color correlation. Future time-domain studies focusing on whether these slowly rotating stars are radial velocity variables are crucial to test the roles of stellar rotation and binarity in generating the split MSs.

Keywords: stars: rotation — open clusters and associations: individual: NGC 2422 — galaxies: star clusters: general.

1. INTRODUCTION

Studies based on Hubble Space Telescope (*HST*) and *Gaia* observations have revealed that many star clusters younger than 2 Gyr exhibit extended main-sequence turnoffs (eMSTOs; e.g., Mackey et al. 2008; Milone et al. 2009,

2018; Cordoni et al. 2018; Li et al. 2019). Clusters younger than 600 Myr also present split main sequences (MSs; Milone et al. 2016, 2018; Correnti et al. 2017; Li et al. 2017; Sun et al. 2019b). The presence of eMSTOs and split MSs in clusters has challenged the scenario that clusters are ‘simple stellar populations’ whose color–magnitude diagrams (CMDs) can be described by a single isochrone characterized by a unique age and metallicity. The eMSTOs were initially thought to be the result of an extended star formation history (eSFH) within the clusters (e.g., Milone et al. 2009; Goudfrooij et al. 2009, 2011), lasting 150–500 Myr in intermediate-age clusters. This scenario, however, attracted lots of objections, such as regarding the absence of gas in Magellanic Cloud (MC) young massive clusters (YMCs; Bastian & Strader 2014), and relating to the morphologies of the sub-giant branches (SGBs) and/or red clumps (RCs) in some massive clusters disfavoring an eSFH (Li et al. 2014a,b, 2016; Bastian & Niederhofer 2015). Another scenario attributes eMSTOs and split MSs to different stellar rotation rates (e.g., Bastian & de Mink 2009; Milone et al. 2018; Cordoni et al. 2018; Sun et al. 2019a,b). The reduction in self-gravity due to rotation will reduce the stellar surface temperature, leading stars to appear redder than their slowly rotating counterparts (von Zeipel 1924). This so-called ‘gravity darkening’ effect works more significantly at stellar equators than at their poles, and thus the observed color of a fast rotating star also depends on its inclination. Another effect, rotational mixing, could expand the stellar convective core, prolonging the MS lifetime of fast rotating stars (Maeder & Meynet 2000). Both effects, caused by stellar rotation, will complicate the morphologies of the MS and MSTO regions of a ‘simple stellar population’ cluster.

Only MS dwarfs less massive than $\sim 1.5M_{\odot}$ are slow rotators because of the magnetic braking effect (Kraft 1967). Because massive MS dwarfs cannot survive in older clusters, if eMSTOs and split MSs are caused by stellar rotation, then only clusters younger than a critical age would exhibit eMSTOs and split MSs. This was confirmed by Milone et al. (2018), who found that only MS stars more massive than $1.6M_{\odot}$ could populate a bifurcated MS. For the eMSTO phenomenon, spectroscopic studies of the Large Magellanic Cloud (LMC) clusters NGC 1866 (~ 200 Myr) and NGC 1846 (~ 1.5 Gyr), and the Galactic open cluster NGC 5822 (~ 0.9 Gyr), have revealed that the average projected rotational velocity, $v \sin i$, of stars on the red side of the MS is higher than that of stars on the blue side (Dupree et al. 2017; Kamann et al. 2020; Sun et al. 2019a). In addition, a significant fraction of Be stars are detected around the MSTO regions of some young MC clusters (e.g., Milone et al. 2018; Bastian et al. 2017), and these Be stars are much redder than normal stars near the MSTO region (Milone et al. 2018).

The split MSs can be ideally reproduced by two coeval stellar populations with different rotational rates, i.e., fast/slow rotating stars populate the red/blue sequences (D’Antona et al. 2015; Milone et al. 2016; D’Antona et al. 2017). Additional evidence comes from spectroscopic analyses of clusters in the LMC and the Milky Way. Marino et al. (2018b) found that the blue and red MS (bMS and rMS) stars in the 40 Myr-old YMC NGC 1818 in the LMC exhibit an obvious difference in $v \sin i$. This bimodality of $v \sin i$ is detected among the eMSTO stars of the intermediate-age LMC cluster NGC 1846 (~ 1.5 Gyr) (Kamann et al. 2020) as well. Using photometry and high-resolution spectra, Marino et al. (2018a) found that a nearby young (~ 300 Myr-old) cluster NGC 6705 exhibits an eMSTO and a broadened MS, and its bMS and rMS are populated by slowly and fast rotating stars. Sun et al. (2019b) analyzed the $v \sin i$ distribution along the well-separated MS of a young Galactic cluster NGC 2287 (~ 200 Myr), and found it shows strong evidence of a bimodal distribution of stellar absolute rotation rates.

The origin of the dichotomy in stellar rotation rates is yet to be examined. To fully explain the morphology of eMSTOs, an age difference between two populations with different rotation rates is required (Milone et al. 2016, 2017; Correnti et al. 2017; Goudfrooij et al. 2017, 2018; Li et al. 2019). D’Antona et al. (2017) suggested that stars on the bMS could be produced by slow rotators that were initially rapidly rotating stars and then were braked within a timescale of less than 25% of the cluster age. This also helps to explain the apparent age differences among eMSTO stars. They proposed that tidal locking in close binaries is responsible for the braking. On the other hand, Bastian et al. (2020) argued that the bimodal distribution of stellar rotational velocities might manifest itself at the pre-main-sequence (PMS) stage, possibly introduced by different disk-locking mechanisms during the PMS phase. Recently, Kamann et al. (2021) detected similar binary fractions in the slow and rapidly rotating stars along the split MS of the massive LMC cluster NGC 1850 (~ 100 Myr). Combined with the similar binary fractions detected in the slow and fast rotating stars at the eMSTO of NGC 1846 by Kamann et al. (2020), Kamann et al. (2021) argue that bimodal rotational distributions are not predominantly caused by binary-induced braking. Recently, Wang et al. (2022) suggested a binary-merger origin for the formation of slow rotators on the blue MS, which is reflected by the unusual mass functions of the bMS stars they detected in NGC 1755, NGC 330, NGC 1818, and NGC 2164.

In this paper, we report on another Galactic open cluster, NGC 2422, which exhibits a bifurcated MS. It cannot be explained by photometric uncertainties or differential reddening, which leaves stellar rotation or/and unresolved binaries as possible explanations. The bifurcated MS of NGC 2422 thus provides a rare opportunity to constrain the effects of stellar rotation and binarity. We studied the eMSTO and split-MS stars of NGC 2422 based on *Gaia* Early Data Release 3 (EDR3; [Gaia Collaboration et al. 2016, 2021](#)). We obtained and resolved high- and medium-resolution spectra of individual stars along the split MS. The aim of this study is to examine whether stars along the cluster’s split MSs also follow a similar correlation between their $v \sin i$ and photometric colors as seen for NGC 2287 ([Sun et al. 2019b](#)).

This article is organized as follows. In Section 2 we describe the data reduction. The main results, as well as their scientific implications are presented in Section 3. In Section 4, we briefly discuss our results and summarize our conclusions.

2. DATA REDUCTION

2.1. Member Star Selection

We obtained *Gaia* EDR3 astrometric and photometric measurements of stars within 2° (≈ 16.87 pc, for a distance to NGC 2422 of ~ 483 pc; [Gaia Collaboration et al. 2018](#)) of the center of NGC 2422 (center coordinates from [Cantat-Gaudin & Anders 2020](#)). The reference epoch for *Gaia* EDR3 is J2016.0. We determined whether they were NGC 2422 members by examining their stellar proper motions $(\mu_\alpha \cos \delta, \mu_\delta)$ and parallaxes (ϖ). In Fig. 1(a), the diagram of stellar proper motions shows that NGC 2422 members are well separated and concentrated at $(\mu_\alpha \cos \delta, \mu_\delta) \approx (-7.0, 1.0)$ mas yr $^{-1}$ ([Gaia Collaboration et al. 2018](#)). We calculated the number density of stars, ρ , in Fig. 1(a) in grids of $(0.1 \text{ mas yr}^{-1})^2$ for stars within $\sqrt{(\mu_\alpha \cos \delta - (-7.0))^2 + (\mu_\delta - 1.0)^2} < 1.5 \text{ mas yr}^{-1}$ (green dashed circle in Fig. 1(a)). The average proper motion of the stars (green dots in the inset of Fig. 1(a)), enclosed by the isodensity contour of $\rho = 2000 \text{ yr}^2 \text{ mas}^{-2}$, $(\mu_\alpha \cos \delta, \mu_\delta) = (-7.06, 1.02)$ mas yr $^{-1}$, was used as the center for selecting cluster members based on their proper motions¹. Based on spectra of 57 FGK stars, [Bailey et al. \(2018\)](#) reported the 1σ dispersion of the radial velocities (RVs) of NGC 2422 stars, $0.750 \pm 0.065 \text{ km s}^{-1}$, whose 3σ dispersion corresponds to $0.98_{-0.09}^{+0.08} \text{ mas yr}^{-1}$ for $\mu_\alpha \cos \delta$ and μ_δ at the distance of NGC 2422, if the motions of member stars in different directions are isotropic. We thus constrained the member stars to have $\sqrt{(\mu_\alpha \cos \delta - (-7.06))^2 + (\mu_\delta - 1.02)^2} < 0.98 \text{ mas yr}^{-1}$ (within the blue dotted circle in Fig. 1(a)), which resulted in a population of 3015 candidate member stars.

We further constrained the cluster members by their stellar ϖ . In Fig. 1(b) and its inset, the NGC 2422 members are concentrated at ~ 2.1 mas (~ 476 pc), which is consistent with the ϖ of the cluster from [Gaia Collaboration et al. \(2018\)](#) (~ 2.069 mas, ~ 483 pc). We first selected stars that have $1.8 \text{ mas} < \varpi < 2.4 \text{ mas}$ (corresponding to a distance range from 417 pc to 555 pc) from the 3015 candidate member stars and calculated the mean (ϖ_a) and standard dispersion (σ_ϖ) of their ϖ . For stars with $G < 17$ mag, we confined the member stars to have ϖ within $\varpi_a \pm \sigma_\varpi$, while for fainter stars ($G > 17$ mag), ϖ had to be within $\varpi_a \pm 3\sigma_\varpi$ because of the larger typical parallax measurement error for fainter stars ([Gaia Collaboration et al. 2021](#)). We then calculated ϖ_a and σ_ϖ for the remaining stars and repeated this process until the variations in ϖ_a and σ_ϖ between subsequent iterations were smaller than 1% of the mean error in ϖ of stars with $G < 17$ mag. We finally identified 1126 stars as NGC 2422 members. Their average stellar proper motion and ϖ are $(\mu_\alpha \cos \delta, \mu_\delta) \approx (-7.05, 1.02)$ mas yr $^{-1}$ and 2.10 mas (~ 476 pc), respectively, which is close to that reported by [Gaia Collaboration et al. \(2018\)](#). The standard dispersions of the $\mu_\alpha \cos \delta$, μ_δ and ϖ of the members stars are 0.33 mas yr^{-1} , 0.32 mas yr^{-1} , and 0.12 mas , respectively. Fig. 1(c) presents the CMD of selected cluster members, along with that of field stars. In Fig. 1(c), the eMSTO and the split MS are visible in the region for $G < 12$ mag. Fig. 1(d) magnifies the loci of the MS within the dashed box in Fig. 1(c) where the split feature is most evident. This pattern is obvious in the 150 Myr-old LMC cluster NGC 1844 and a Galactic open cluster NGC 2287 as well ([Milone et al. 2013; Sun et al. 2019b](#)). We confirmed that photometric uncertainties were not responsible for the split pattern of the MS (see Fig. 1(d)). In Fig. 2, we show the split MS regions in NGC 2422 and NGC 2287. The widths of the split features in both clusters are comparable.

2.2. Isochrone Fitting

¹ In the inset of Fig. 1(a), three populations have $\rho > 2000 \text{ yr}^2 \text{ mas}^{-2}$. We only used the most centrally concentrated population with respect to the green dashed circle to determine the circle’s center to constrain the proper motions of the member stars. The other two populations were excluded because they are closer to the concentration of the proper motions of the field stars, which may introduce additional contamination

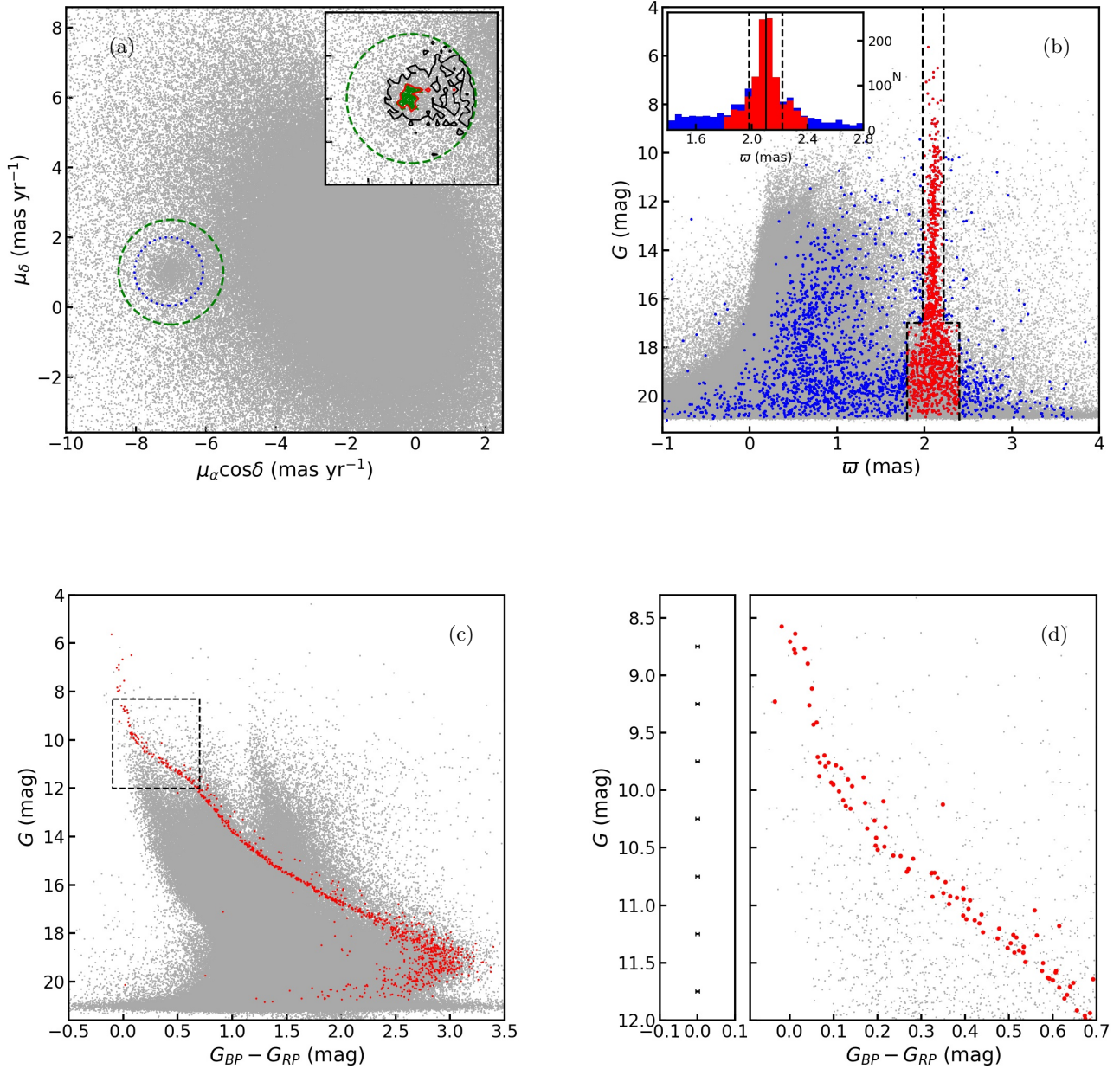


Figure 1. (a) Selection of NGC 2422 cluster members based on their stellar proper motions (see the text for details). The inset shows the isodensity contours at $\rho = 1000 \text{ yr}^2 \text{ mas}^{-2}$ (black) and $\rho = 2000 \text{ yr}^2 \text{ mas}^{-2}$ (red) of stars within the green dashed circle. (b) Distribution of the parallaxes (ϖ) as a function of *Gaia* G -band magnitudes of cluster members (red dots), candidate members selected only based on proper motions (blue dots), and field stars (grey dots). The corresponding number distributions are shown using the same colors in the inset, except for the field stars. The dashed polygon encloses the ϖ range of the cluster members. The solid and dashed vertical lines in the inset show ϖ_a of the cluster members and the range of $\varpi_a \pm \sigma_\varpi$, respectively. (c) CMD of the member stars (red dots) and the field stars (grey dots). (d) Magnified view of the CMD within the dashed box in panel (c), where the split pattern is most evident. The left subpanel shows the mean uncertainties in the G magnitudes and $G_{BP} - G_{RP}$ colors in the corresponding G magnitude ranges.

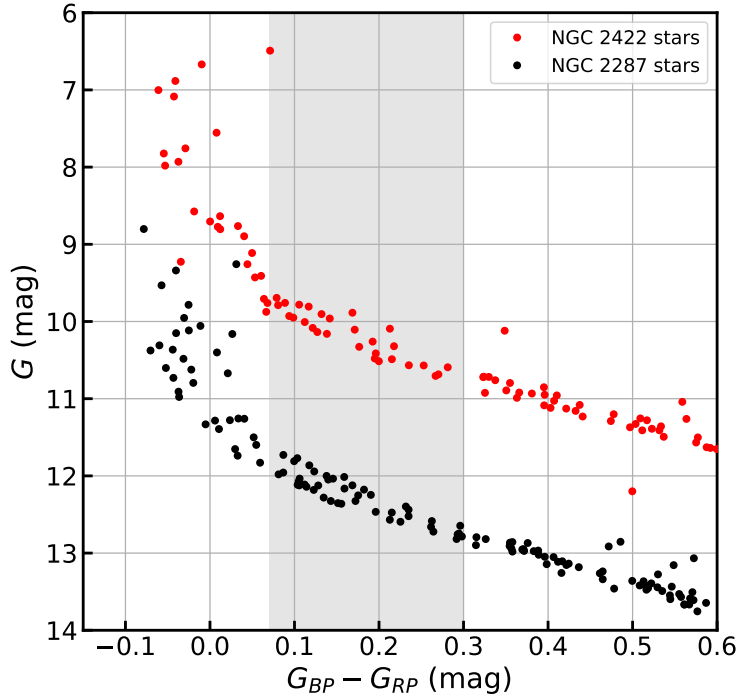


Figure 2. Comparison of the split MS regions of NGC 2422 (red dots) and NGC 2287 (black dots). To separate their split MSs, the CMD of NGC 2287 was shifted up by one magnitude along the ordinate. The grey area highlights the region where their split patterns are most evident.

We used isochrones from the PARSEC model (version 1.2S, [Marigo et al. 2017](#)) to fit the CMD of NGC 2422. In [Fig. 3](#), the CMD of NGC 2422 is fitted by a set of isochrones for metallicity $Z = 0.0133$ ($Z_{\odot} = 0.0152$ in the PARSEC model) and extinction $A_V = 0.3$ mag for a distance modulus $(m - M)_0 = 8.29$ mag. [Bailey et al. \(2018\)](#) obtained $[\text{Fe}/\text{H}] = -0.05 \pm 0.02$ dex for NGC 2422, corresponding to $Z = 0.0135 \pm 0.0006$, which is similar to the metallicity of the isochrones in [Fig. 3](#). Their distance modulus corresponds to a distance of ~ 455 pc, which is close to the distance inferred from the average parallax of the cluster members. The extinction coefficients for the *Gaia* bands were derived following [Cardelli et al. \(1989\)](#), adopting the [O’Donnell \(1994\)](#) $R_V = 3.1$ extinction curve. The ages of the isochrones range from 90 Myr to 170 Myr in steps of 20 Myr, matching an age spread of 80 Myr to fit the width of the MSTO. The best-fitting isochrone to the blue edge of the MSTO region has an age of 90 Myr, identified by visual inspection. The age of NGC 2422 in the literature spans a wide range. [Kharchenko et al. \(2013\)](#) derived an age of 132 Myr, while [Loktin et al. \(2001\)](#) gave an age of only 73 Myr. This difference in age estimates for NGC 2422 is expected. Because of the presence of an eMSTO, the absence of a red-giant branch also complicates the determination of an accurate isochronal age. Differential reddening may affect the morphology of the MSTO region as well ([Platais et al. 2012](#)). To examine the effect of differential reddening, we shifted the best-fitting isochrone by ± 0.02 mag in color (see [Fig. 3](#)), which correspond to the three times the measurement errors in the stellar colors for stars within the inset of [Fig. 3](#). As shown by that inset figure, most stars on the MS ridgeline reside within the region limited by the shifted best-fitting isochrones. This indicates that the effect of differential reddening on the CMD of NGC 2422 is limited. It is thus unlikely responsible for the appearance of the eMSTO and the split MS.

2.3. Spectroscopic Data Reduction

We obtained spectra of 36 A-type stars in NGC 2422 from Canada–France–Hawaii’i Telescope (CFHT) program 20BS002, observed with ESPaDOnS with a resolution of $R \approx 68,000$ and a signal-to-noise ratio (SNR) of ~ 80 at \sim

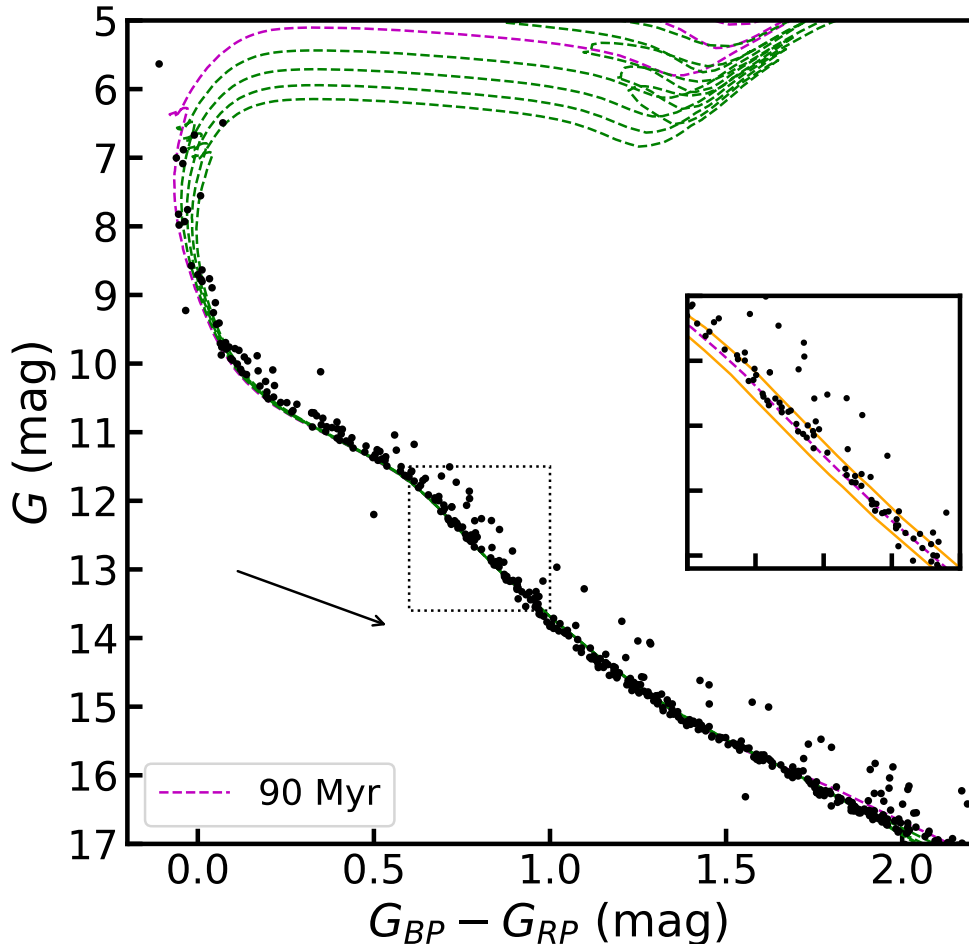


Figure 3. CMD of NGC 2422 member stars (black dots) based on *Gaia* EDR3. Isochrones of ages ranging from 90 Myr to 170 Myr in steps of 20 Myr are shown as dashed lines. The magenta dashed line shows the best-fitting isochrone to the blue edge of the eMSTO, with an age 90 Myr, $A_V = 0.3$ mag, $Z = 0.0133$, and a distance modulus $(m - M)_0 = 8.29$ mag. Other isochrones are shown as green dashed lines. The black arrow represents the reddening vector, corresponding to $\Delta A_V = 1.0$ mag. The inset shows the MS region used to test for differential reddening, where the solid orange lines are obtained by shifting the best-fitting isochrone (dashed magenta line) by ± 0.02 mag in color.

4440 Å. We also observed spectra of 22 A- and F-type stars with the Southern African Large Telescope (SALT; Buckley et al. 2006) through program 2019-2-SCI-023 with a resolution of $R \approx 4000$ and a SNR of ~ 200 at a wavelength of 4884.4 Å. Eleven stars were observed with both the CFHT and SALT. In total, we have 47 spectroscopic sample objects to investigate the $v \sin i$ of stars along the split MS. Information about their magnitudes and the observation facilities is summarized in Table 1.

We classified our 47 sample stars into four groups based on their positions in the CMD (Fig. 4). For stars with $G > 9.5$ mag, the 24 and 13 stars on the left and right sides of the split MS are classified as bMS and rMS stars, respectively. In Fig. 4, the equal-mass binary sequence has been plotted by shifting the best-fitting isochrone by -0.75 mag in the *Gaia* G band. We identified one star beyond the equal-mass binary sequence, which may be caused by photometric errors due to inaccurate point-spread-function fitting residuals, or it may be a triple system. For stars with $G < 9.5$ mag, the bMS, rMS, and equal-mass ratio binary sequence are too close to be clearly separated. The 9 stars in this magnitude range are defined as upper MS (uMS) stars.

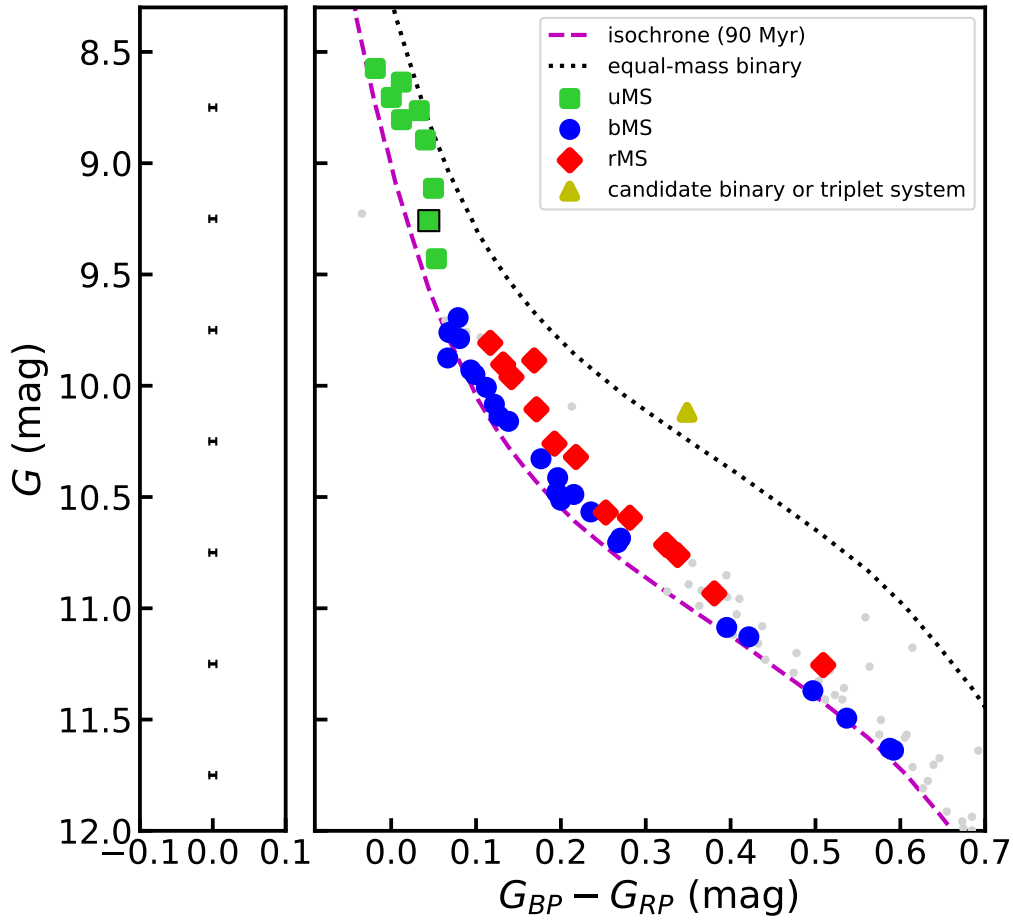


Figure 4. The bMS, rMS, and uMS stars are labeled with solid blue circles, red diamonds, and green squares, respectively. The candidate binary or triplet system located near the equal-mass sequence (the dotted black line) is represented by a solid yellow triangle. The double-lined spectroscopic binary system is labeled with an open square. The magenta dashed line represents the best-fitting isochrone. The light grey dots are other member stars for which we do not have spectra. In the left panel, we show the mean uncertainties for the G magnitudes and $G_{BP} - G_{RP}$ colors of stars in each G -magnitude bin of 0.5 mag.

To measure the stellar projected rotational velocities, $v \sin i$, we generated a series of synthetic stellar spectra for a range of parameters (stellar effective temperatures T_{eff} , $\log g$, $[\text{Fe}/\text{H}]$, $v \sin i$, and RVs) to fit the observed absorption profiles of the Mg II line ($\sim 4481 \text{ \AA}$) for the CFHT spectra, and the H_{β} (4861 \AA) and Mg I triplet ($5100\text{-}5200 \text{ \AA}$) for the SALT spectra. Synthetic stellar spectra were derived from the Pollux database (Palacios et al. 2010), with T_{eff} ranging from 6000 K to 15,000 K (in steps of 100 K), surface gravities from $\log g = 3.5$ to $\log g = 5.0$ (in steps of 0.1 dex), and $[\text{Fe}/\text{H}]$ from -1.0 dex to 1.0 dex (in steps of 0.5 dex). Plane-parallel ATLAS12 model atmospheres in local thermodynamic equilibrium were used to generate the corresponding synthetic spectra (Kurucz 2005). A fixed microturbulent velocity of 2 km s^{-1} was introduced using the tool SYNSPEC (Hubeny & Lanz 1992). Since the step in $[\text{Fe}/\text{H}]$ of the derived synthetic spectra is large, we fixed $[\text{Fe}/\text{H}]$ at 0.0 dex in our spectroscopic fitting, based on the metallicity of our best-fitting isochrone (close to Z_{\odot} in the PARSEC model) and the $[\text{Fe}/\text{H}]$ detected by Bailey et al. (2018) for NGC 2422 members (see Section 2.2). We used PyAstronomy (Czesla et al. 2019) to convolve the synthetic

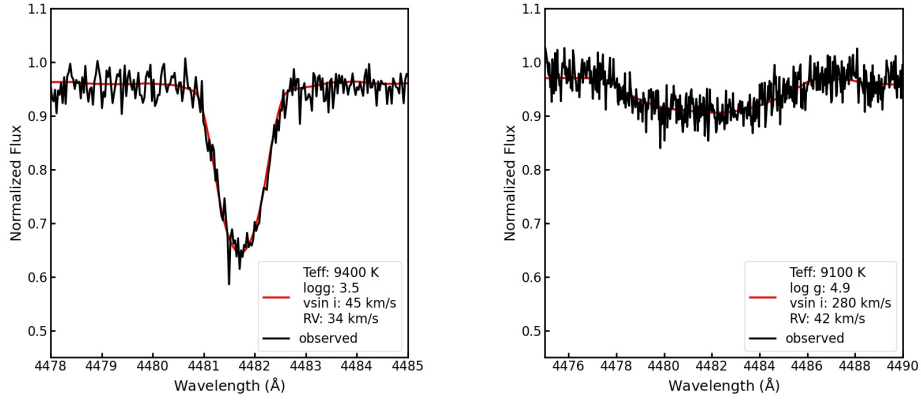


Figure 5. Two example spectra of a slowly rotating star (left), and a fast rotating star (right), along with their best-fitting models (red solid lines). Best-fitting parameters are shown in each legend.

spectra with the effects of instrumental and rotating ($v \sin i$) broadening, and shift the wavelengths based on RVs. The instrumental resolution of CFHT was simulated for the synthetic spectra with a Gaussian kernel of $\sigma_c \approx 0.029 \text{ \AA}$, whereas that of SALT was estimated through the width of the corresponding arc line. The $v \sin i$ values ranged from 5 km s^{-1} to 400 km s^{-1} in steps of 5 km s^{-1} . RVs ranged from 0 km s^{-1} to 70 km s^{-1} in steps of 2 km s^{-1} , corresponding to the average RV of the 57 NGC 2422 FGK stars ($35.97 \pm 0.09 \text{ km s}^{-1}$) measured by Bailey et al. (2018). Then the synthetic flux of the model spectra corresponding to each wavelength value of the observed spectra was calculated with the tool Astrolib PySynphot (STScI Development Team 2013). We compared the generated models with the observed absorption-line profiles and derived the best-fitting T_{eff} , $\log g$, $[\text{Fe}/\text{H}]$, $v \sin i$, and RV for each star using a minimum- χ^2 method. For the SALT data, we further used a Monte Carlo method (Foreman-Mackey et al. 2013) to estimate the uncertainty in $v \sin i$ around the grid values. In Fig. 5, we show the spectra of a fast rotating star and a slowly rotating star, along with their best-fitting models.

We confirmed that the uncertainties in T_{eff} and $\log g$, which were estimated based on the stars' color-magnitude loci, have minor effects on their $v \sin i$ determination. Our analysis confirmed that stars observed by both the CFHT and SALT yielded similar results, as shown in Fig. 6. The average of the measured $v \sin i$ from the CFHT and SALT data was taken as the $v \sin i$ measurement result for each common target. For the data observed with CFHT, the $v \sin i$ uncertainties were estimated through mock spectra combined with the χ^2 minimization method (Avni 1976; Wall 1996; de Grijs et al. 2013), with a 1σ uncertainty corresponding to the difference between the $v \sin i$ values for χ^2_{min} (the minimum χ^2) and $\chi^2_{\text{min}} + 1$. For each common target, we took the uncertainty of the CFHT data as their $v \sin i$ measurement uncertainty. For stars observed only with SALT, their average 1σ uncertainty of the $v \sin i$ measurement was $\sim 10 \text{ km s}^{-1}$. We included the 2σ uncertainties for each star in Table 1.

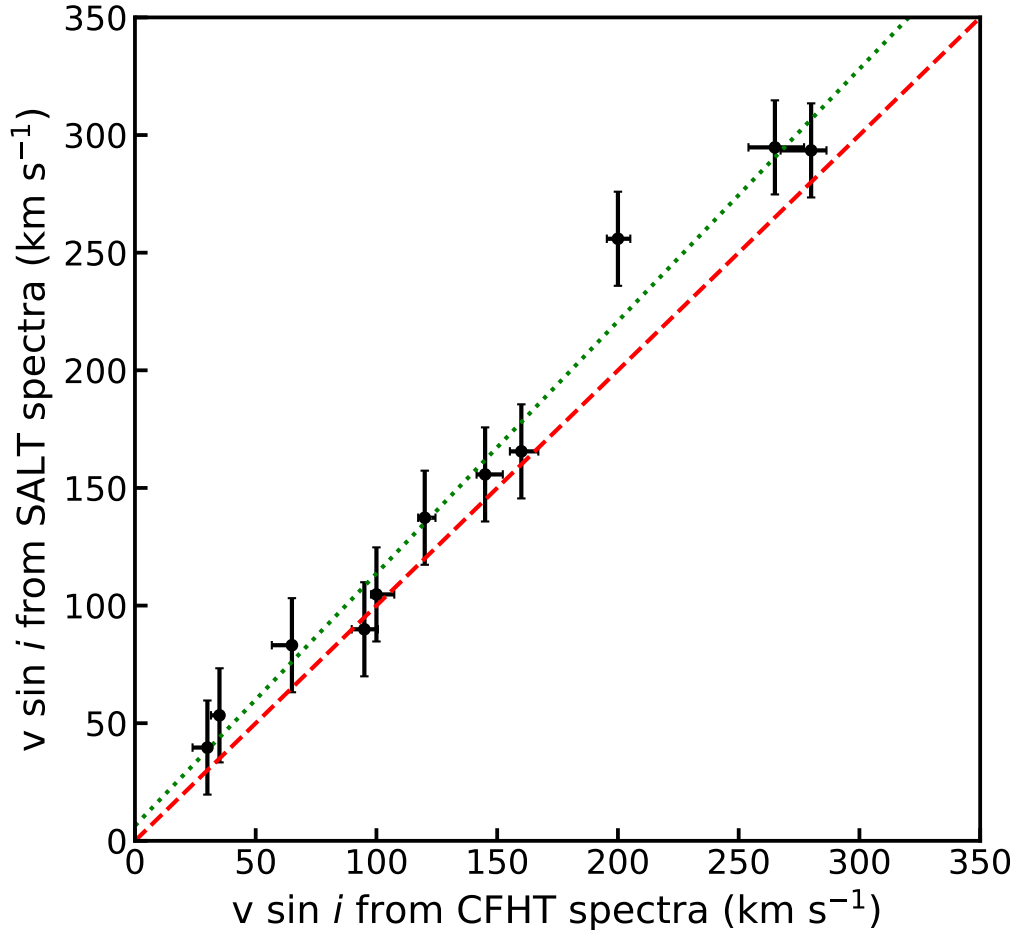


Figure 6. Comparison of derived $v \sin i$ values from CFHT and SALT spectra for 11 stars observed with both facilities (black dots). The error bars show the 2σ uncertainties presented in Table 1. The red dashed line is the equal-value track. The dotted green line shows the best-fitting line for the data points, representing the function of $v \sin i_{\text{SALT}} = 1.07v \sin i_{\text{CFHT}} + 6.40 \text{ km s}^{-1}$, where $v \sin i_{\text{SALT}}$ and $v \sin i_{\text{CFHT}}$ denote the projected rotation rates measured from the spectra observed with SALT and CFHT, respectively.

3. MAIN RESULTS AND DISCUSSION

In Table 1, we present the derived projected rotation velocities for our 47 sample stars with their errors. The distribution of $v \sin i$ spans the range from 5.0 km s^{-1} to 325.0 km s^{-1} . We present the CMD of the 47 stars in Fig. 7, with their $v \sin i$ color-coded. In Fig. 8(a), we plot the distribution of stellar color deviations, $\Delta(G_{\text{BP}} - G_{\text{RP}})$, versus their projected rotational velocities, $v \sin i$. The color deviation is defined as the difference of a star's color ($G_{\text{BP}} - G_{\text{RP}}$) from that of the best-fitting isochrone. In Fig. 8(a), we have excluded the candidate triple system. From Fig. 8(a) we see that the stellar color deviation indeed exhibits a bimodal distribution, which again demonstrates the presence of a bifurcated MS. The $v \sin i$ distribution does not exhibit a bimodal distribution as clearly as that of the color deviation distribution, although it appears to be demarcated around $v \sin i \sim 200 \text{ km s}^{-1}$. The average $v \sin i$ for bMS stars is $\sim 100 \text{ km s}^{-1}$ with a standard deviation of $\sim 54 \text{ km s}^{-1}$, and most (23/24) bMS stars have $v \sin i \leq 175 \text{ km s}^{-1}$. The $v \sin i$ distribution of the 13 rMS stars is broader, with a mean and standard dispersion of $\sim 146 \text{ km s}^{-1}$ and

$\sim 98 \text{ km s}^{-1}$, respectively. Impressively, 9 out of the 13 rMS stars have $v \sin i < 160 \text{ km s}^{-1}$, rotating with $v \sin i$ like those of most bMS stars, except for 4 rMS stars rotating fast with $v \sin i > 250 \text{ km s}^{-1}$ (see Fig. 8). Fig. 8(a) does not present any evident correlation between the stellar projected rotation rates and the stellar color deviations for the split-MS stars. The Spearman correlation coefficient between the color deviation and $v \sin i$ of the bMS and rMS stars is 0.18, for $p = 0.28$, while it is 0.55 (Marino et al. 2018a) and 0.68 (Sun et al. 2019b) for NGC 6705 and NGC 2287, respectively. We further tested the hypothesis that the $v \sin i$ of the rMS and bMS stars of NGC 2422 are generated from the same distribution with the Anderson-Darling test for k-samples. The result shows a significance level of ~ 0.21 , indicating that the hypothesis can not be rejected. To compare with NGC 2422, we also conducted Anderson-Darling tests for the $v \sin i$ of the bMS and rMS stars of NGC 1818 (Marino et al. 2018b), NGC 6705 (Marino et al. 2018a) and NGC 2287 (Sun et al. 2019b). Their tests all reported significance levels smaller than 0.001, implying that the $v \sin i$ distributions of the bMS and rMS stars of each of these three clusters are different. Therefore, the bMS and rMS stars of NGC 2422 are not strongly correlated with slowly and fast rotating populations, respectively, which is very different to the cases in NGC 1818 (Marino et al. 2018b), NGC 6705 (Marino et al. 2018a) and NGC 2287 (Sun et al. 2019b).

Table 1. Photometric information and projected rotational velocities of NGC 2422 stars

<i>Gaia</i> ID	<i>G</i> (mag)	<i>G</i> _{RP} (mag)	<i>G</i> _{BP} (mag)	$\Delta(G_{\text{BP}} - G_{\text{RP}})$	$v \sin i$ (km s ⁻¹) ^a	Classification	Facility
(1)	(2)	(3)	(4)	(5)	(6)	(7)	(8)
3030259479295155072	8.57	8.55	8.57	0.009	$55^{+3.31}_{-2.50}$	uMS	CFHT
3030228413786622720	8.64	8.63	8.61	0.037	$325^{+16.89}_{-6.68}$	uMS	CFHT
3030027447983067008	8.70	8.69	8.69	0.021	$102^{+7.39}_{-2.25}$	uMS	CFHT & SALT
3030013257412699264	8.76	8.76	8.73	0.050	$45^{+0.21}_{-7.90}$	uMS	CFHT
3029930553522238208	8.80	8.80	8.78	0.026	$125^{+2.61}_{-5.43}$	uMS	CFHT
3030024286886910080	8.90	8.90	8.86	0.049	$225^{+13.01}_{-7.63}$	uMS	CFHT
3029917801751039104	9.11	9.12	9.07	0.043	$245^{+6.30}_{-4.99}$	uMS	CFHT
3028387801268979584	9.26	9.26	9.22	0.026	$40^{+4.98}_{-6.31}$	uMS	CFHT
3030028925451798400	9.43	9.44	9.38	0.020	$228^{+5.13}_{-4.60}$	uMS	CFHT & SALT
3030681004563366016	9.69	9.71	9.64	0.021	$175^{+4.15}_{-6.09}$	bMS	CFHT
3030035350722750592	9.76	9.78	9.71	0.004	$163^{+7.04}_{-4.74}$	bMS	CFHT & SALT
3030004530036746368	9.79	9.81	9.73	0.013	$145^{+5.18}_{-4.98}$	bMS	CFHT
3030030746517945600	9.88	9.89	9.83	-0.012	$45^{+5.88}_{-2.41}$	bMS	CFHT
3030228692968781824	9.93	9.96	9.86	0.009	$155^{+6.09}_{-3.30}$	bMS	CFHT
3030034732247423360	9.95	9.98	9.88	0.011	$115^{+8.13}_{-2.12}$	bMS	CFHT
3030645957629616384	10.01	10.04	9.93	0.017	$225^{+9.31}_{-10.68}$	bMS	CFHT
3030219140961660416	10.08	10.12	10.00	0.016	$130^{+18.47}_{-9.47}$	bMS	CFHT
3029232707231846784	10.14	10.18	10.05	0.013	$100^{+1.07}_{-8.55}$	bMS	CFHT
3030038546178432256	10.16	10.20	10.06	0.020	$74^{+1.30}_{-8.32}$	bMS	CFHT & SALT
3030035522521452032	10.33	10.39	10.21	0.028	$150^{+7.33}_{-3.54}$	bMS	CFHT & SALT
3030027207464910976	10.41	10.48	10.28	0.029	$129^{+4.45}_{-2.74}$	bMS	CFHT & SALT
3030015215917673088	10.48	10.54	10.35	0.013	$35^{+0.39}_{-6.14}$	bMS	CFHT & SALT
3029919592765618304	10.49	10.56	10.35	0.031	$92^{+5.61}_{-5.23}$	bMS	CFHT & SALT
3030069263785446400	10.51	10.58	10.38	0.009	$25^{+4.13}_{-0.20}$	bMS	CFHT
3030313802042017536	10.57	10.65	10.41	0.030	$65^{+6.22}_{-16.98}$	bMS	CFHT

Table 1 continued on next page

Table 1 (continued)

<i>Gaia</i> ID	<i>G</i> (mag)	<i>G</i> _{RP} (mag)	<i>G</i> _{BP} (mag)	$\Delta(G_{\text{BP}} - G_{\text{RP}})$	$v \sin i$ (km s ⁻¹) ^a	Classification	Facility
(1)	(2)	(3)	(4)	(5)	(6)	(7)	(8)
3030015662586533888	10.68	10.78	10.51	0.031	44 ^{+0.88} _{-3.52}	bMS	CFHT & SALT
3030026588989698048	10.70	10.80	10.53	0.021	55 ^{+9.90} _{-0.15}	bMS	CFHT
3030016109262918016	11.09	11.23	10.83	0.010	71 ± 20.00	bMS	SALT
3030014219483828864	11.13	11.28	10.86	0.020	153 ± 20.00	bMS	SALT
3030014013325413248	11.37	11.55	11.06	0.006	92 ± 20.00	bMS	SALT
3030026138007337088	11.49	11.69	11.15	0.003	104 ± 20.00	bMS	SALT
3030025661276778880	11.63	11.85	11.26	0.012	5 ⁺²⁰ ₋₅	bMS	SALT
3030028444415416704	11.64	11.86	11.27	0.014	52 ± 20.00	bMS	SALT
3030231785345188608	9.81	9.84	9.72	0.047	80 ^{+4.22} _{-3.85}	rMS	CFHT
3030250751920573696	9.89	9.94	9.77	0.089	30 ^{+3.70} _{-0.23}	rMS	CFHT
3029983914193883648	9.90	9.94	9.81	0.050	130 ^{+6.95} _{-3.18}	rMS	CFHT
3030033495296943488	9.96	10.00	9.86	0.052	110 ^{+3.30} _{-6.00}	rMS	CFHT
3030015662592785664	10.11	10.16	9.99	0.062	280 ^{+12.08} _{-10.95}	rMS	CFHT & SALT
3030298374519750912	10.26	10.32	10.13	0.057	15 ^{+8.76} _{-0.52}	rMS	CFHT
3030034972765597440	10.32	10.39	10.17	0.070	287 ^{+6.36} _{-12.66}	rMS	CFHT & SALT
3033318767322824704	10.57	10.66	10.40	0.047	135 ^{+7.72} _{-1.83}	rMS	CFHT
3030085756457512832	10.59	10.69	10.41	0.069	160 ^{+3.40} _{-6.71}	rMS	CFHT
3029932821264851968	10.71	10.83	10.51	0.075	299 ± 20.00	rMS	SALT
3030028684933623808	10.76	10.88	10.54	0.074	55 ± 20.00	rMS	SALT
3030016143629067904	10.93	11.07	10.69	0.054	252 ± 20.00	rMS	SALT
3030022152277677440	11.26	11.44	10.94	0.061	59 ± 20.00	rMS	SALT
3029931068918279296	10.12	10.24	9.89	0.237	134 ± 20.00	binary	SALT

^aThe errors shown correspond to 2 σ uncertainties.

NOTE—(1) *Gaia* ID in EDR3; (2, 3, 4) *Gaia* bands; (5) Color deviations; (6) Projected rotational velocities; (7) Stellar classification; (8) Observation facilities.

Taking NGC 2287 as a comparison, NGC 2422 contains a higher fraction of slowly rotating stars in its rMS, which reduces the correlation between their $v \sin i$ and color deviations. Only 25% of the NGC 2287 rMS stars have $v \sin i < 160$ km s⁻¹ (Sun et al. 2019b), while this ratio is over 69% (9/13) for NGC 2422. Although most bMS stars are slowly rotating stars, the presence of the high fraction of stars with low $v \sin i$ is not consistent with the rotation scenario.

We now discuss the effects of stellar inclinations and binarity. The projected rotational velocities depend on both the absolute rotational velocities, v , and the stellar inclination, i . If we assume that split-MS stars are single stars, the stellar rotation scenario suggests that rMS should be populated by fast rotating stars. They may exhibit small $v \sin i$ values if their inclinations are small. Slowly/non-rotating stars will never populate the rMS, however. Based on this consideration, the only explanation which accounts for the rMS stars with low $v \sin i$ is that their inclinations are low. Based on the isochrones including stellar rotation from the SYCLIST database (Georgy et al. 2013), we find that the absolute rotational velocities of stars with $1.7M_{\odot} < M < 2.5M_{\odot}$ (the estimated mass range of the rMS stars) are about 210 km s⁻¹ to 280 km s⁻¹ at an age of 90 Myr. Based on this result, four rMS stars with 250 km s⁻¹ $< v \sin i < 300$ km s⁻¹ should rotate with an edge-on spin-axis. We explored whether a uniform distribution of spin-axis directions in three-dimensional space can reproduce the observed $v \sin i$ of the rMS stars. We generated 10,000 synthetic stars with a uniform distribution of v within 200 km s⁻¹ and 300 km s⁻¹ and stochastic orientations

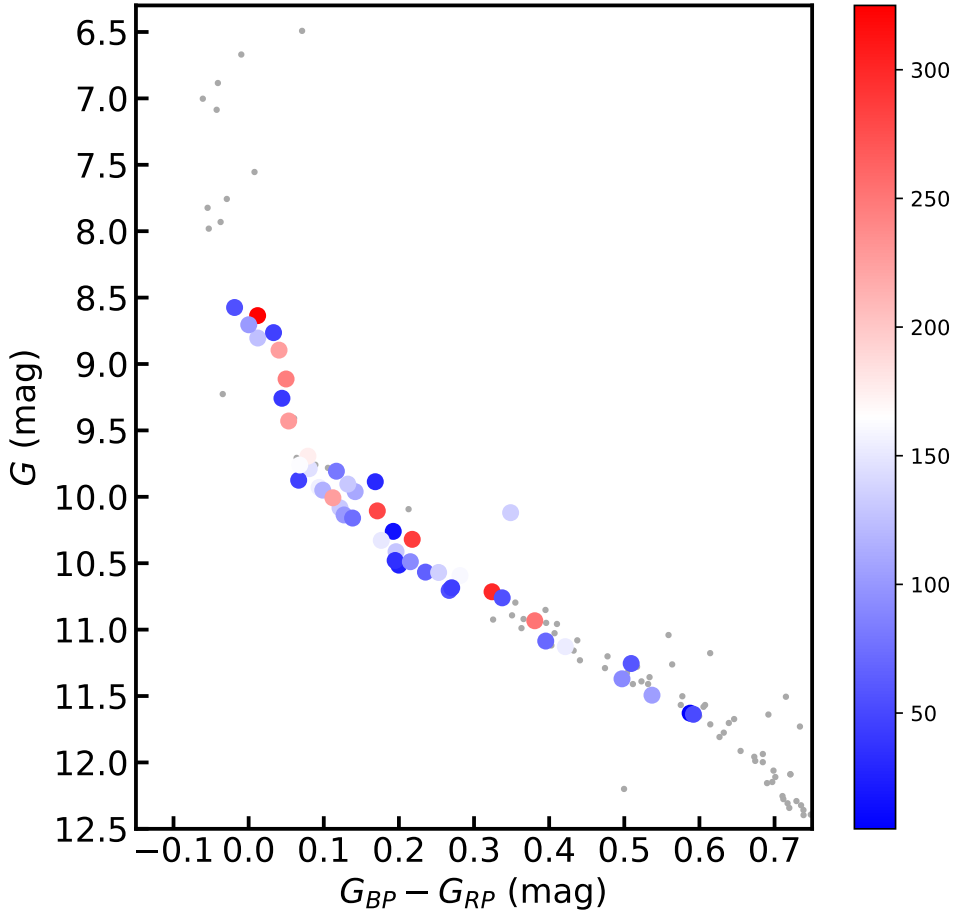


Figure 7. CMD of the 47 stars with $v \sin i$ measurements (color-coded)

of their spin axes in three-dimensional space (generated from a uniform distribution in $\cos i$ following [Lim et al. 2019](#)). Fig. 9 shows the normalized $v \sin i$ distribution of the rMS stars and that of our 10,000 synthetic stars in an example run. We visually excluded the possibility that stochastic orientations of the spin axes can generate the observed $v \sin i$. However, we emphasize that small-number statistics may introduce a large uncertainty. To resolve stellar inclinations from projected rotational velocities, asteroseismological studies are required to derive their absolute rotational velocities.

Another important factor that may affect our analysis is the presence of unresolved binaries. To observe a tight correlation between the stellar rotational velocities and their colors requires that most bMS stars are single stars or low mass-ratio binaries. Otherwise, they will contaminate the rMS region, since unresolved high mass-ratio binaries tend to be located on the red side of the MS. [D’Antona et al. \(2017\)](#) suggested that bMS stars are slow rotators that spin fast at birth, whose rotation rates are then braked within 25% of a cluster’s age, and tidal locking in close binaries could be responsible for this braking. If the tidal-locking scenario is correct, the photometry of some slow rotators is possibly contaminated by hidden binary companions that shift their loci in the red (and bright) direction. These hidden companions may explain the appearance of the slow rotators in the rMS. Unresolved binaries may also lead to broadened or split profiles of absorption lines in stellar spectra. In our spectra, we only found one double-lined

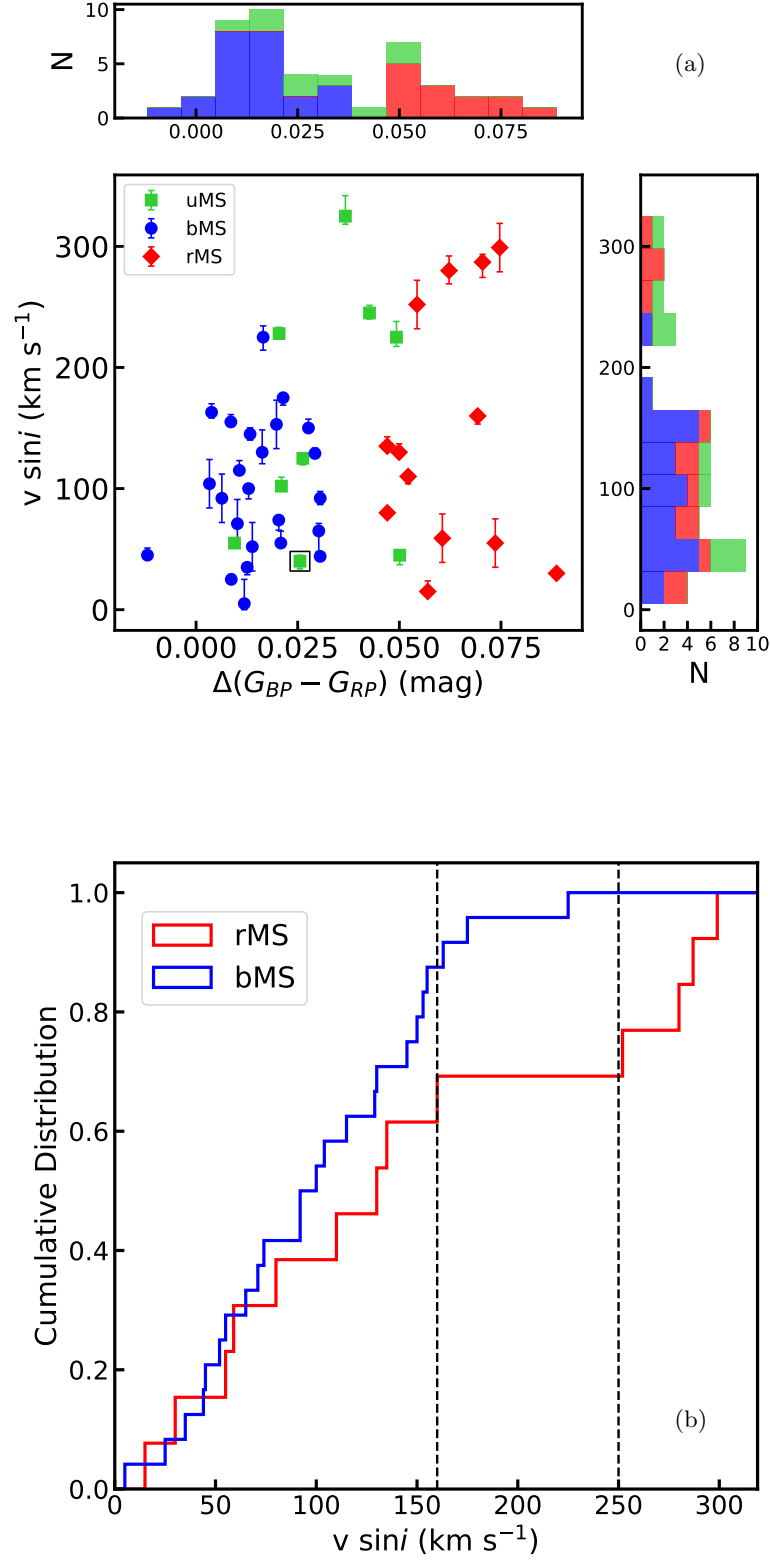


Figure 8. (a) Stellar $v \sin i$ (including the 2σ uncertainties) versus stellar color deviations, $\Delta(G_{BP} - G_{RP})$, of the bMS, rMS, and uMS stars. The distributions of the color deviations and $v \sin i$ are shown in the top and right panels. The double-lined spectroscopic binary system is enclosed by an open square. (b) Cumulative distributions of $v \sin i$ for bMS and rMS stars. The two dashed vertical lines represent $v \sin i = 160 \text{ km s}^{-1}$ (left) and 250 km s^{-1} (right), respectively.

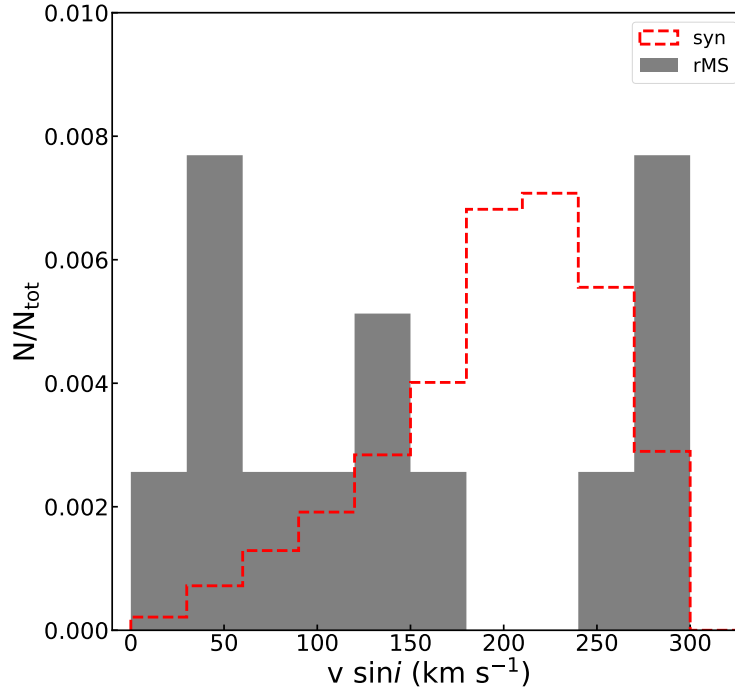


Figure 9. Normalized distribution of the $v \sin i$ of 10,000 synthetic stars (red dashed line) for a flat distribution of v within the range of 200 km s^{-1} and 300 km s^{-1} , and a uniform distribution of the directions of the spin axes in a run, along with the $v \sin i$ distribution of rMS stars (grey bars)

spectroscopic binary system that exhibited an additional absorption profile at $\sim 4479 \text{ \AA}$ near that of the primary star (at $\sim 4482 \text{ \AA}$, *Gaia* ID: 3028387801268979584; for its position in the CMD and information about its $v \sin i$ and color deviation, see Fig. 4 and Fig. 8(a), respectively), which may indicate the presence of a companion. It has a slow projected rotational rate ($v \sin i = 40^{+4.98}_{-6.31} \text{ km s}^{-1}$), which is consistent with the prediction of the tidal-locking scenario. Intriguingly, this star was found to be a variable star (Hackstein et al. 2015). We did not detect any clear signatures of unresolved binaries in any of our other spectra.

We explored if some MS stars may hide a binary companion using the Binary Information from Open Clusters Using SEDs (BINOCS) package (Thompson & Frinchaboy 2015; Thompson et al. 2021). BINOCS was specifically designed for determining accurate component masses for unresolved binaries by fitting observed magnitudes from synthetic stellar SEDs (Thompson & Frinchaboy 2015; Thompson et al. 2021). Unresolved binaries’ SEDs would have an excess of infrared flux compared with single stars if they hide a low-mass companion star (Thompson et al. 2021). In BINOCS, observed magnitudes from at least three optical, three near-infrared, and two mid-infrared filters are a prerequisite (Thompson et al. 2021). In addition to the *Gaia* G_{BP} , G , and G_{RP} magnitudes, which serve as optical inputs, for each star we obtained their corresponding 2MASS JHK_s (Skrutskie et al. 2006) and WISE [3.6] and [4.5] passbands (Wright et al. 2010) as our near- and mid-infrared inputs, respectively. Theoretical stellar SEDs of single and binary stars (with different mass ratios, q) were generated based on the parameters implied by the best-fitting isochrone from the PARSEC model. Then, the observed magnitudes were directly compared with the synthetic stellar SEDs. BINOCS has different q thresholds for binary stars of different primary masses (Thompson et al. 2021). In the mass range explored here, only stars with mass ratios $q > 0.3$ are identified as binaries.

We analyzed the binarity for a total of 109 stars. They were composed of 32 stars from the bMS and rMS stars with $v \sin i < 200 \text{ km s}^{-1}$ and 77 stars located below the split MS within the range from $11.50 \text{ mag} < G < 13.60 \text{ mag}$ to

$0.67 \text{ mag} < G_{\text{BP}} - G_{\text{RP}} < 0.98 \text{ mag}$. Both populations have complete photometric data for the eight input passbands. We excluded five fast-rotating split-MS stars with $v \sin i > 200 \text{ km s}^{-1}$ from our SED fitting analysis, because the colors of these stars may be strongly affected by the gravity darkening effect caused by their fast rotation. BINOCs is not accurate for the determination of the binarity of stars located where the best-fitting isochrone and equal-mass ratio binary sequence are close (Thompson et al. 2021). Therefore, we did not explore the binarity of the uMS stars based on SED fitting. The loci of the SED-fitting samples in the CMD and the fitting result are shown in Fig. 10.

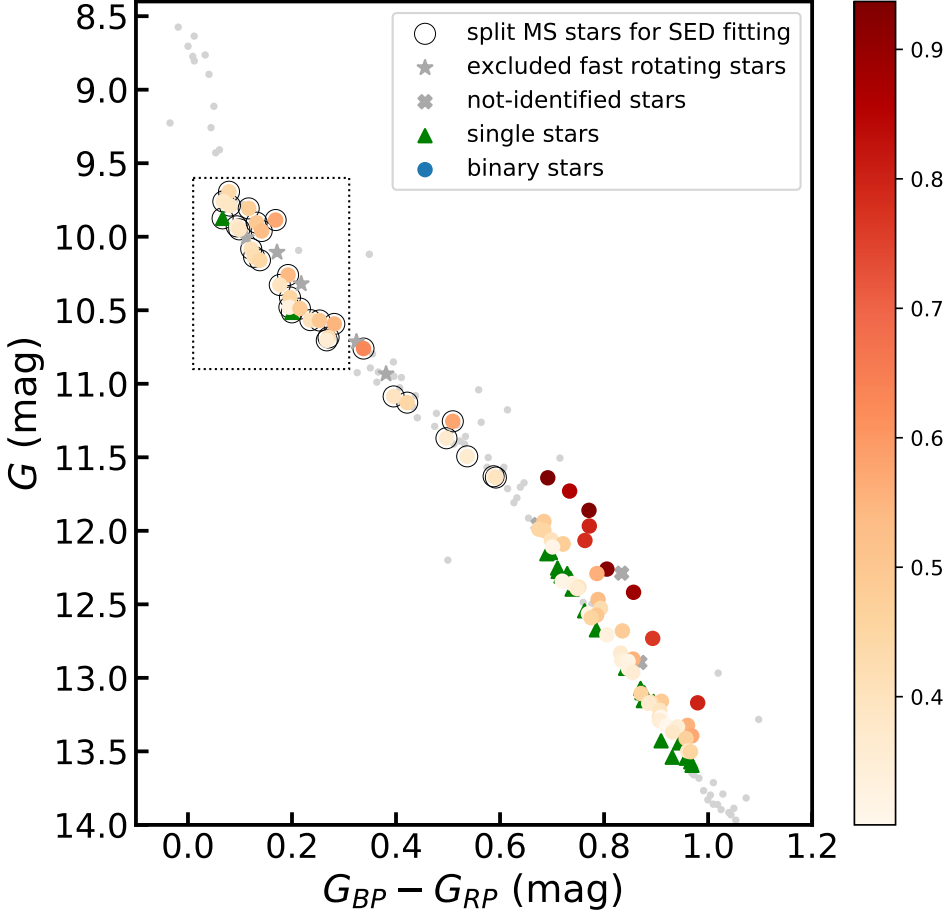


Figure 10. CMD of the 109 stars used for our binarity analysis. Stars surrounded by open circles are the 32 bMS and rMS stars used for SED fitting. Grey star labels show targets discarded from the binarity analysis because of their high rotational velocities. The dotted box shows the region where 87% of stars have been analyzed spectroscopically. Single and binary stars verified by BINOCs are represented by green triangles and solid points, respectively, color-coded by the derived mass ratios. Three lower-MS stars with a binarity that cannot be determined through SED fitting are marked by grey crosses. Small grey dots are other cluster member stars for which spectroscopy is not available or which lack complete photometric data in the eight prerequisite passbands.

We determined a binary number fraction for the lower-MS stars of at least $\sim 65\%$ (50/77, while the binarity of three lower-MS stars cannot be identified; see Fig. 10), which is consistent with the binary fraction of $62 \pm 16\%$ predicted by Bailey et al. (2018). Thirty of the 32 split-MS objects are identified as unresolved binaries. We further analyzed

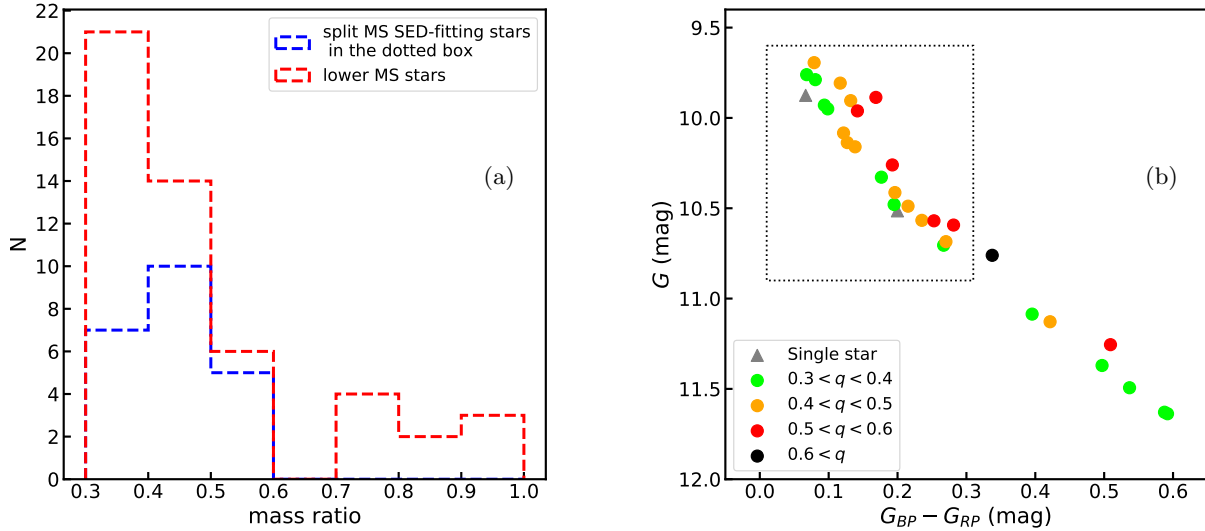


Figure 11. (a) Histograms of the binary mass-ratio distributions of the sample objects subjected to SED fitting located within the dashed box in Fig. 10 (blue dashed lines) and lower-MS stars (red dashed lines). (b) CMD of the 32 split-MS stars used for SED fitting, classified based on their derived mass ratios. The dotted box shows the same region as that in Fig. 10.

stars within the range from $9.6 \text{ mag} < G < 10.9 \text{ mag}$ to $0.01 \text{ mag} < (G_{BP} - G_{RP}) < 0.31 \text{ mag}$ (see the dotted box in Fig. 10) where 87% (27/31) of the members have been explored spectroscopically. In this range, 22 of the 24 objects were identified as unresolved binaries, indicating a higher binary number fraction of at least $\sim 81\%$ (22/27, if we assume that the three fast rotators are single stars) along the split MS than that along the lower MS. Fig. 11(a) presents the binary mass-ratio distributions for the split and lower-MS samples. Intriguingly, we find that both the split and lower-MS stars lack high mass-ratio binaries ($q > 0.6$). This may indicate that the mass-ratio distribution of stars in this MS range favors a low mass-ratio dominated shape, similar to that derived by Kouwenhoven et al. (2007) for OB associations. We are cautious about this conclusion, however, because at the distance of NGC 2422, many wide binary systems in this MS range might have been resolved. In Fig. 11(b), we find that most rMS stars with $v \sin i < 200 \text{ km s}^{-1}$ have mass ratios within the range $0.4 < q < 0.6$. This indicates that unresolved binaries with these mass ratios can populate the rMS.

However, we emphasize that this analysis only proves that unresolved binaries can explain the red colors of some rMS stars. It does not mean that they are genuine binaries. Strong gravity darkening caused by fast rotation can alter the distributions of the effective temperatures on the stellar surfaces and change the stellar SEDs. Therefore, both varying stellar rotation rates and inclinations of the spin axes would influence the capability of BINOCS to identify unresolved binaries from rotating stars. For stars located below the split MS, this effect is negligible because stars along the lower MS are usually slow rotators because of the magnetic braking effect (Kraft 1967). To test the effect of rotation on BINOCS for split-MS stars, we fitted synthetic SEDs of mock stars ($1.7M_{\odot} < M < 2.5M_{\odot}$) with different absolute rotation rates, using the theoretical photometry provided by the isochrones for rotating stars from the SYCLIST database (Georgy et al. 2013). We found that BINOCS could correctly identify the binarity of stars at a confidence level of at least $83.1 \pm 3.6\%$ for stars with absolute rotation rates smaller than $\sim 130 \text{ km s}^{-1}$ ². We note that about 75% (24/32) of our sample objects along the split MS have $v \sin i \leq 130 \text{ km s}^{-1}$. For the rMS stars, this ratio is $\sim 78\%$ (7/9). This indicates that they might be slowly rotating stars for which stellar rotation did not significantly change their SEDs. However, we cannot conclude that they are genuine binaries at a high confidence level due to a lack of information about their inclinations. To examine if these stars have binary origins, time-domain studies of their radial velocities or light curves are mandatory.

² In our fits of the mock SEDs, only three optical passbands (*Gaia* G_{BP} , G , and G_{RP}) and three near-infrared passbands (2MASS JHK_s) were used because of the limitation of the isochrones. This may decrease the correction ratio for BINOCS to separate single from binary stars.

4. CONCLUSIONS

D’Antona et al. (2017) suggested that the population of slowly rotating stars may hide binary companions. These stars may initially have been fast rotating stars that have spun down due to early-stage tidal interactions. Assuming that their hypothesis can account for the presence of slowly rotating stars in NGC 2422, we estimated the synchronization timescales, τ_{sync} , for 10 slowly-rotating stars with $v \sin i \leq 100 \text{ km}^{-1}$ within the dotted box in Fig. 10. Following Hurley et al. (2002), we estimated τ_{sync} for stars with radiative envelopes,

$$\frac{1}{\tau_{\text{sync}}} = 52^{5/3} \left(\frac{GM}{R^3} \right)^{1/2} \frac{MR^2}{I} q^2 (1+q)^{5/6} E_2 \left(\frac{R}{a} \right)^{17/2}, \quad (1)$$

where G is the gravitational constant and M and R are the primary star’s mass and radius, respectively. a is the separation of the binary components, q denotes the mass ratio, and I is the moment of inertia. The units used in the equation are in the CGS system. E_2 is a second-order tidal coefficient that can be fitted to values given by Zahn (1975),

$$E_2 = 1.592 \times 10^{-9} M^{2.84}, \quad (2)$$

where M is in units of M_{\odot} . To estimate the synchronization timescales, we used M and q derived from the SED fitting. We estimated R based on the empirical relation, $R \approx 1.33 \times M^{0.555}$ for stars with $M > 1.66 M_{\odot}$ (Demircan & Kahraman 1991).

In Fig. 12, we present the calculated synchronization timescales as a function of a/R . Our calculation shows that the mean synchronization timescale dramatically increases with increasing binary separation relative to their radii, a/R . From Fig. 12, we can estimate that if most slowly rotating stars are tidally locked on timescales less than the cluster’s age, their separation would not exceed 4.5 times the primary star’s radius, $a/R < 4.5$. This indicates that at least 21% (10/47) of our spectroscopically explored sample objects are tidally interacting binaries, which accounts for 37% (10/27) of the spectroscopically explored split-MS stars within the dotted box in Fig. 10. We estimated the orbital periods, P , of the companions for 10 stars using Kepler’s third law, assuming $a/R = 4.5$. This gives $P = 2.13_{-0.08}^{+0.12}$ days for these stars. However, Moe & Di Stefano (2017) showed that fewer than 10% of binaries with A- and late-B primary stars ($2M_{\odot} < M < 5M_{\odot}$) have companion periods shorter than 10 days, and such a high fraction of 37% of close binaries with $P < 10$ days is only efficient for O-type MS stars ($M > 16M_{\odot}$). We thus argue that the high fraction of tidally interacting binaries detected in the split MS is unusual. Whether or not these slowly rotating stars hide such compact companions deserves further investigation.

In summary, we have reported on a Galactic open cluster with a bifurcated MS, NGC 2422, using photometric data from *Gaia* EDR3. We measured projected rotational velocities, $v \sin i$, for 47 stars along the split MS of NGC 2422, using high- and medium-resolution spectra observed with CFHT and SALT, respectively. We found a weak correlation between $v \sin i$ and color, which is inconsistent with the stellar rotation scenario. This is caused by the presence of a significant fraction of slowly rotating stars among the rMS stars. If these rMS stars do not have a specific inclination distribution, their red colors can be explained by unresolved binaries. If the presence of slowly rotating stars is not primordial, but if they were tidally braked by interacting binaries, (as suggested by D’Antona et al. 2017), their maximum separations would not exceed five times their primary star’s radius. This would indicate that 37% of objects in the split MS are tidally interacting binaries. Such a high fraction, if it is not primordial, is unusual when compared with observations. Time-domain measurements of the RVs of these slow rotators are crucial to reveal whether NGC 2422 is rich in close binaries.

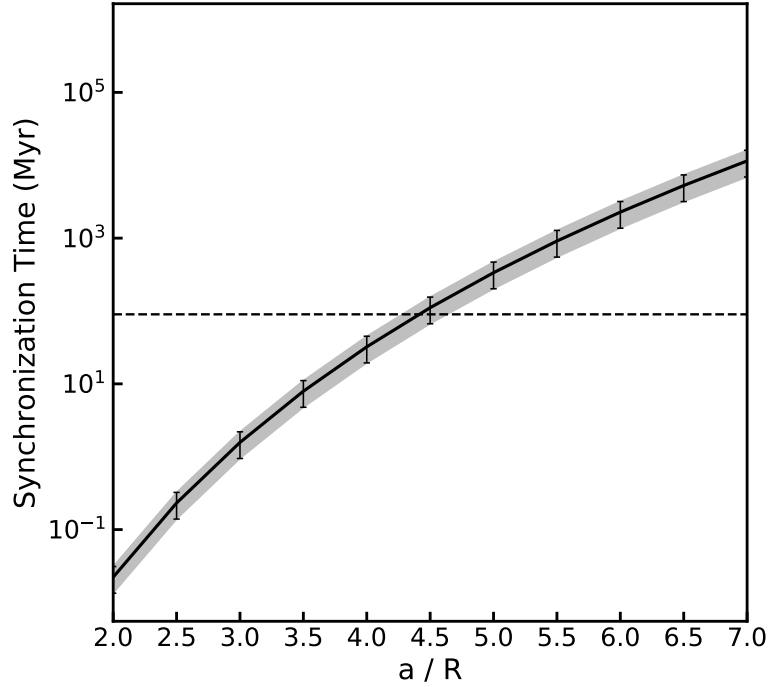


Figure 12. Mean synchronization timescales versus different binary separations a/R for the 10 slowly rotating stars ($v \sin i < 100 \text{ km s}^{-1}$) located within the dotted box of Fig. 10. The grey shade represents the 1σ standard deviation of the synchronization time. The dashed line indicates 90 Myr, i.e., the best-fitting age of NGC 2422.

We acknowledge the anonymous referee and the statistics editor of the American Astronomical Society Journals for their very useful suggestions. This work was supported by the National Natural Science Foundation of China (NSFC) through grant 12073090. This research was also supported in part by the Australian Research Council Centre of Excellence for All Sky Astrophysics in 3 Dimensions (ASTRO 3D), through project CE170100013. This research uses data obtained through the Telescope Access Program (TAP), which has been funded by the TAP member institutes. We acknowledge the science research grants from the China Manned Space Project with NO. CMS-CSST-2021-A08. L.C. and J.Z. acknowledge support from the National Natural Science Foundation of China (NSFC) through grants 12090040 and 12090042. L.L. and Z.S. acknowledge support from the National Natural Science Foundation of China (NSFC) grant U2031139 and the National Key R&D Program of China grant No. 2019YFA0405501. This work has made use of data from the European Space Agency (ESA) mission *Gaia* (<https://www.cosmos.esa.int/gaia>), processed by the *Gaia* Data Processing and Analysis Consortium (DPAC, <https://www.cosmos.esa.int/web/gaia/dpac/consortium>). Funding for the DPAC has been provided by national institutions, in particular the institutions participating in the *Gaia* Multilateral Agreement. This research has used the POLLUX database (<http://pollux.oreme.org>), operated at LUPM (UniversitMontpellier-CNRS, France, with the support of the PNPS and INSU. This publication has made use of data products from the Two Micron All Sky Survey, which is a joint project of the University of Massachusetts and the Infrared Processing and Analysis Center/California Institute of Technology, funded by the National Aeronautics and Space Administration and the National Science Foundation. This publication also makes use of data products from the Wide-field Infrared Survey Explorer, which is a joint project of the University of California, Los Angeles, and the Jet Propulsion Laboratory/California Institute of Technology, funded by the National Aeronautics and Space Administration.

Software: PARSEC (1.2S; Marigo et al. 2017), Astropy (Astropy Collaboration et al. 2013, 2018), Matplotlib (Hunter 2007), SciPy (Virtanen et al. 2020), SYNSPEC (Hubeny & Lanz 1992), PyAstronomy (Czesla et al. 2019, <https://github.com/sczesla/PyAstronomy>), Astrolib PySynphot (STScI Development Team 2013), SYCLIST (Georgy et al. 2013), BINOCS (Thompson & Frinchaboy 2015; Thompson et al. 2021), TOPCAT (Taylor 2005)

REFERENCES

- Astropy Collaboration, Robitaille, T. P., Tollerud, E. J., et al. 2013, *A&A*, 558, A33, doi: [10.1051/0004-6361/201322068](https://doi.org/10.1051/0004-6361/201322068)
- Astropy Collaboration, Price-Whelan, A. M., Sipőcz, B. M., et al. 2018, *AJ*, 156, 123, doi: [10.3847/1538-3881/aabc4f](https://doi.org/10.3847/1538-3881/aabc4f)
- Avni, Y. 1976, *ApJ*, 210, 642, doi: [10.1086/154870](https://doi.org/10.1086/154870)
- Bailey, J. I., Mateo, M., White, R. J., Shectman, S. A., & Crane, J. D. 2018, *MNRAS*, 475, 1609, doi: [10.1093/mnras/stx3266](https://doi.org/10.1093/mnras/stx3266)
- Bastian, N., & de Mink, S. E. 2009, *MNRAS*, 398, L11, doi: [10.1111/j.1745-3933.2009.00696.x](https://doi.org/10.1111/j.1745-3933.2009.00696.x)
- Bastian, N., Kamann, S., Amard, L., et al. 2020, *MNRAS*, 495, 1978, doi: [10.1093/mnras/staa1332](https://doi.org/10.1093/mnras/staa1332)
- Bastian, N., & Niederhofer, F. 2015, *MNRAS*, 448, 1863, doi: [10.1093/mnras/stv116](https://doi.org/10.1093/mnras/stv116)
- Bastian, N., & Strader, J. 2014, *MNRAS*, 443, 3594, doi: [10.1093/mnras/stu1407](https://doi.org/10.1093/mnras/stu1407)
- Bastian, N., Cabrera-Ziri, I., Niederhofer, F., et al. 2017, *MNRAS*, 465, 4795, doi: [10.1093/mnras/stw3042](https://doi.org/10.1093/mnras/stw3042)
- Buckley, D. A. H., Swart, G. P., & Meiring, J. G. 2006, in *Society of Photo-Optical Instrumentation Engineers (SPIE) Conference Series*, Vol. 6267, Society of Photo-Optical Instrumentation Engineers (SPIE) Conference Series, ed. L. M. Stepp, 62670Z, doi: [10.1117/12.673750](https://doi.org/10.1117/12.673750)
- Cantat-Gaudin, T., & Anders, F. 2020, *A&A*, 633, A99, doi: [10.1051/0004-6361/201936691](https://doi.org/10.1051/0004-6361/201936691)
- Cardelli, J. A., Clayton, G. C., & Mathis, J. S. 1989, *ApJ*, 345, 245, doi: [10.1086/167900](https://doi.org/10.1086/167900)
- Cordoni, G., Milone, A. P., Marino, A. F., et al. 2018, *ApJ*, 869, 139, doi: [10.3847/1538-4357/aaedc1](https://doi.org/10.3847/1538-4357/aaedc1)
- Correnti, M., Goudfrooij, P., Bellini, A., Kalirai, J. S., & Puzia, T. H. 2017, *MNRAS*, 467, 3628, doi: [10.1093/mnras/stx010](https://doi.org/10.1093/mnras/stx010)
- Czesla, S., Schröter, S., Schneider, C. P., et al. 2019, *PyA: Python astronomy-related packages*. <http://ascl.net/1906.010>
- D'Antona, F., Di Criscienzo, M., Decressin, T., et al. 2015, *MNRAS*, 453, 2637, doi: [10.1093/mnras/stv1794](https://doi.org/10.1093/mnras/stv1794)
- D'Antona, F., Milone, A. P., Tailo, M., et al. 2017, *Nature Astronomy*, 1, 0186, doi: [10.1038/s41550-017-0186](https://doi.org/10.1038/s41550-017-0186)
- de Grijs, R., Li, C., Zheng, Y., et al. 2013, *ApJ*, 765, 4, doi: [10.1088/0004-637X/765/1/4](https://doi.org/10.1088/0004-637X/765/1/4)
- Demircan, O., & Kahraman, G. 1991, *Ap&SS*, 181, 313, doi: [10.1007/BF00639097](https://doi.org/10.1007/BF00639097)
- Dupree, A. K., Dotter, A., Johnson, C. I., et al. 2017, *ApJL*, 846, L1, doi: [10.3847/2041-8213/aa85dd](https://doi.org/10.3847/2041-8213/aa85dd)
- Foreman-Mackey, D., Hogg, D. W., Lang, D., & Goodman, J. 2013, *PASP*, 125, 306, doi: [10.1086/670067](https://doi.org/10.1086/670067)
- Gaia Collaboration, Prusti, T., de Bruijne, J. H. J., et al. 2016, *A&A*, 595, A1, doi: [10.1051/0004-6361/201629272](https://doi.org/10.1051/0004-6361/201629272)
- Gaia Collaboration, Babusiaux, C., van Leeuwen, F., et al. 2018, *A&A*, 616, A10, doi: [10.1051/0004-6361/201832843](https://doi.org/10.1051/0004-6361/201832843)
- Gaia Collaboration, Brown, A. G. A., Vallenari, A., et al. 2021, *A&A*, 649, A1, doi: [10.1051/0004-6361/202039657](https://doi.org/10.1051/0004-6361/202039657)
- Georgy, C., Ekström, S., Granada, A., et al. 2013, *A&A*, 553, A24, doi: [10.1051/0004-6361/201220558](https://doi.org/10.1051/0004-6361/201220558)
- Goudfrooij, P., Girardi, L., Bellini, A., et al. 2018, *ApJL*, 864, L3, doi: [10.3847/2041-8213/aada0f](https://doi.org/10.3847/2041-8213/aada0f)
- Goudfrooij, P., Girardi, L., & Correnti, M. 2017, *ApJ*, 846, 22, doi: [10.3847/1538-4357/aa7fb7](https://doi.org/10.3847/1538-4357/aa7fb7)
- Goudfrooij, P., Puzia, T. H., Chandar, R., & Kozhurina-Platais, V. 2011, *ApJ*, 737, 4, doi: [10.1088/0004-637X/737/1/4](https://doi.org/10.1088/0004-637X/737/1/4)
- Goudfrooij, P., Puzia, T. H., Kozhurina-Platais, V., & Chandar, R. 2009, *AJ*, 137, 4988, doi: [10.1088/0004-6256/137/6/4988](https://doi.org/10.1088/0004-6256/137/6/4988)
- Hackstein, M., Fein, C., Haas, M., et al. 2015, *Astronomische Nachrichten*, 336, 590, doi: [10.1002/asna.201512195](https://doi.org/10.1002/asna.201512195)
- Hubeny, I., & Lanz, T. 1992, *A&A*, 262, 501
- Hunter, J. D. 2007, *Computing in Science and Engineering*, 9, 90, doi: [10.1109/MCSE.2007.55](https://doi.org/10.1109/MCSE.2007.55)
- Hurley, J. R., Tout, C. A., & Pols, O. R. 2002, *MNRAS*, 329, 897, doi: [10.1046/j.1365-8711.2002.05038.x](https://doi.org/10.1046/j.1365-8711.2002.05038.x)
- Kamann, S., Bastian, N., Usher, C., Cabrera-Ziri, I., & Saracino, S. 2021, *MNRAS*, 508, 2302, doi: [10.1093/mnras/stab2643](https://doi.org/10.1093/mnras/stab2643)
- Kamann, S., Bastian, N., Gossage, S., et al. 2020, *MNRAS*, 492, 2177, doi: [10.1093/mnras/stz3583](https://doi.org/10.1093/mnras/stz3583)
- Kharchenko, N. V., Piskunov, A. E., Schilbach, E., Röser, S., & Scholz, R. D. 2013, *A&A*, 558, A53, doi: [10.1051/0004-6361/201322302](https://doi.org/10.1051/0004-6361/201322302)
- Kouwenhoven, M. B. N., Brown, A. G. A., Portegies Zwart, S. F., & Kaper, L. 2007, *A&A*, 474, 77, doi: [10.1051/0004-6361:20077719](https://doi.org/10.1051/0004-6361:20077719)

- Kraft, R. P. 1967, *ApJ*, 150, 551, doi: [10.1086/149359](https://doi.org/10.1086/149359)
- Kurucz, R. L. 2005, *Memorie della Societa Astronomica Italiana Supplementi*, 8, 189
- Li, C., de Grijs, R., Bastian, N., et al. 2016, *MNRAS*, 461, 3212, doi: [10.1093/mnras/stw1491](https://doi.org/10.1093/mnras/stw1491)
- Li, C., de Grijs, R., & Deng, L. 2014a, *ApJ*, 784, 157, doi: [10.1088/0004-637X/784/2/157](https://doi.org/10.1088/0004-637X/784/2/157)
- . 2014b, *Nature*, 516, 367, doi: [10.1038/nature13969](https://doi.org/10.1038/nature13969)
- Li, C., de Grijs, R., Deng, L., & Milone, A. P. 2017, *ApJ*, 844, 119, doi: [10.3847/1538-4357/aa7b36](https://doi.org/10.3847/1538-4357/aa7b36)
- Li, C., Sun, W., de Grijs, R., et al. 2019, *ApJ*, 876, 65, doi: [10.3847/1538-4357/ab15d2](https://doi.org/10.3847/1538-4357/ab15d2)
- Lim, B., Rauw, G., Nazé, Y., et al. 2019, *Nature Astronomy*, 3, 76, doi: [10.1038/s41550-018-0619-5](https://doi.org/10.1038/s41550-018-0619-5)
- Loktin, A. V., Gerasimenko, T. P., & Malysheva, L. K. 2001, *Astronomical and Astrophysical Transactions*, 20, 607, doi: [10.1080/10556790108221134](https://doi.org/10.1080/10556790108221134)
- Mackey, A. D., Broby Nielsen, P., Ferguson, A. M. N., & Richardson, J. C. 2008, *ApJL*, 681, L17, doi: [10.1086/590343](https://doi.org/10.1086/590343)
- Maeder, A., & Meynet, G. 2000, *ARA&A*, 38, 143, doi: [10.1146/annurev.astro.38.1.143](https://doi.org/10.1146/annurev.astro.38.1.143)
- Marigo, P., Girardi, L., Bressan, A., et al. 2017, *ApJ*, 835, 77, doi: [10.3847/1538-4357/835/1/77](https://doi.org/10.3847/1538-4357/835/1/77)
- Marino, A. F., Milone, A. P., Casagrande, L., et al. 2018a, *ApJL*, 863, L33, doi: [10.3847/2041-8213/aad868](https://doi.org/10.3847/2041-8213/aad868)
- Marino, A. F., Przybilla, N., Milone, A. P., et al. 2018b, *AJ*, 156, 116, doi: [10.3847/1538-3881/aad3cd](https://doi.org/10.3847/1538-3881/aad3cd)
- Milone, A. P., Bedin, L. R., Cassisi, S., et al. 2013, *A&A*, 555, A143, doi: [10.1051/0004-6361/201220567](https://doi.org/10.1051/0004-6361/201220567)
- Milone, A. P., Bedin, L. R., Piotto, G., & Anderson, J. 2009, *A&A*, 497, 755, doi: [10.1051/0004-6361/200810870](https://doi.org/10.1051/0004-6361/200810870)
- Milone, A. P., Marino, A. F., D'Antona, F., et al. 2016, *MNRAS*, 458, 4368, doi: [10.1093/mnras/stw608](https://doi.org/10.1093/mnras/stw608)
- . 2017, *MNRAS*, 465, 4363, doi: [10.1093/mnras/stw2965](https://doi.org/10.1093/mnras/stw2965)
- Milone, A. P., Marino, A. F., Di Criscienzo, M., et al. 2018, *MNRAS*, 477, 2640, doi: [10.1093/mnras/sty661](https://doi.org/10.1093/mnras/sty661)
- Moe, M., & Di Stefano, R. 2017, *ApJS*, 230, 15, doi: [10.3847/1538-4365/aa6fb6](https://doi.org/10.3847/1538-4365/aa6fb6)
- O'Donnell, J. E. 1994, *ApJ*, 422, 158, doi: [10.1086/173713](https://doi.org/10.1086/173713)
- Palacios, A., Gebran, M., Josselin, E., et al. 2010, *A&A*, 516, A13, doi: [10.1051/0004-6361/200913932](https://doi.org/10.1051/0004-6361/200913932)
- Platais, I., Melo, C., Quinn, S. N., et al. 2012, *ApJL*, 751, L8, doi: [10.1088/2041-8205/751/1/L8](https://doi.org/10.1088/2041-8205/751/1/L8)
- Skrutskie, M. F., Cutri, R. M., Stiening, R., et al. 2006, *AJ*, 131, 1163, doi: [10.1086/498708](https://doi.org/10.1086/498708)
- STScI Development Team. 2013, pynphot: Synthetic photometry software package, Astrophysics Source Code Library, record ascl:1303.023. <http://ascl.net/1303.023>
- Sun, W., de Grijs, R., Deng, L., & Albrow, M. D. 2019a, *ApJ*, 876, 113, doi: [10.3847/1538-4357/ab16e4](https://doi.org/10.3847/1538-4357/ab16e4)
- Sun, W., Li, C., Deng, L., & de Grijs, R. 2019b, *ApJ*, 883, 182, doi: [10.3847/1538-4357/ab3cd0](https://doi.org/10.3847/1538-4357/ab3cd0)
- Taylor, M. B. 2005, in *Astronomical Society of the Pacific Conference Series*, Vol. 347, *Astronomical Data Analysis Software and Systems XIV*, ed. P. Shopbell, M. Britton, & R. Ebert, 29
- Thompson, B. A., & Frinchaboy, P. M. 2015, in *American Astronomical Society Meeting Abstracts*, Vol. 225, *American Astronomical Society Meeting Abstracts #225*, 415.03
- Thompson, B. A., Frinchaboy, P. M., Spoo, T., & Donor, J. 2021, *AJ*, 161, 160, doi: [10.3847/1538-3881/abde4c](https://doi.org/10.3847/1538-3881/abde4c)
- Virtanen, P., Gommers, R., Oliphant, T. E., et al. 2020, *Nature Methods*, 17, 261, doi: [10.1038/s41592-019-0686-2](https://doi.org/10.1038/s41592-019-0686-2)
- von Zeipel, H. 1924, *MNRAS*, 84, 665, doi: [10.1093/mnras/84.9.665](https://doi.org/10.1093/mnras/84.9.665)
- Wall, J. V. 1996, *QJRAS*, 37, 519
- Wang, C., Langer, N., Schootemeijer, A., et al. 2022, *Nature Astronomy*, doi: [10.1038/s41550-021-01597-5](https://doi.org/10.1038/s41550-021-01597-5)
- Wright, E. L., Eisenhardt, P. R. M., Mainzer, A. K., et al. 2010, *AJ*, 140, 1868, doi: [10.1088/0004-6256/140/6/1868](https://doi.org/10.1088/0004-6256/140/6/1868)
- Zahn, J. P. 1975, *A&A*, 41, 329